

Structure of the oxygen-annealed chalcogenide superconductor $\text{Fe}_{1.08}\text{Te}_{0.55}\text{Se}_{0.45}\text{O}_x$

Hefei Hu,^{1,3} Jian-Min Zuo,^{2,3,*} Mao Zheng,^{1,3} James N. Eckstein,^{1,3} Wan Kyu Park,^{1,3} Laura H. Greene,^{1,3} Jinsheng Wen,⁴ Zhijun Xu,⁴ Zhiwei Lin,⁴ Qiang Li,⁴ and Genda Gu⁴

¹*Department of Physics, University of Illinois at Urbana-Champaign, Urbana, Illinois 61801, USA*

²*Department of Materials Science and Engineering, University of Illinois, 1304 W. Green Street, Urbana, Illinois 61801, USA*

³*Frederick Seitz Materials Research Laboratory, University of Illinois at Urbana-Champaign, Urbana, Illinois 61801, USA*

⁴*Condensed Matter Physics and Materials Science Department, Brookhaven National Laboratory, Upton, New York 11973, USA*

(Received 13 October 2011; revised manuscript received 21 December 2011; published 6 February 2012)

The as-grown single crystal $\text{Fe}_{1.08}\text{Te}_{0.55}\text{Se}_{0.45}$ with the tetragonal PbO-type structure is nonsuperconducting owing to the excess Fe. Superconductivity is induced after oxygen annealing with an onset and zero resistance transition temperature around 14.5 K and 11.5 K, respectively. The oxygen doping is evidenced by electron energy loss spectroscopy and accompanied by improved homogeneity in the remaining PbO-type phase, as well as an increase in the L_3/L_2 intensity ratio of the Fe- $L_{2,3}$ edge, indicating an increase in Fe valence. Local phase transformation from the tetragonal PbO-type phase to the hexagonal NiAs-type phase is also observed after oxygen annealing.

DOI: 10.1103/PhysRevB.85.064504

PACS number(s): 74.70.Xa, 61.05.jm, 74.25.fc, 82.80.Pv

I. INTRODUCTION

The discovery of superconductivity in $\text{LaFeAsO}_{1-x}\text{F}_x$ ¹ has attracted significant interest in iron-based superconductors. The family of $\text{FeTe}_{1-x}\text{Se}_x$ materials, which are composed of only Fe(Se/Te) layers, received special attraction due to its simple crystal structure. It has been found that isovalent substitution of Te with Se in the parent compound FeTe induces superconductivity in $\text{FeTe}_{1-x}\text{Se}_x$,² reaching $T_c \sim 15$ K at the optimized doping of 50% Se.² Interestingly, the properties of superconductivity and magnetism in $\text{FeTe}_{1-x}\text{Se}_x$ not only depend on doping level, but also on the Fe content.^{3,4} In the parent compound Fe_{1+y}Te , the commensurate antiferromagnetic order can be tuned into an incommensurately magnetic structure as the content of excess Fe increases.³ Superconductivity in $\text{Fe}_{1+y}\text{Te}_{1-x}\text{Se}_x$ is suppressed and the magnetic correlations increase, as y increases (for $y \geq 0$).⁴ In the other end-member of this family, Fe_{1+y}Se , superconductivity is found to be extremely sensitive to the Fe content, where superconductivity disappears at $y = 0.03$.⁵ It has been reported that annealing $\text{FeTe}_{1-x}\text{Se}_x$ with less excess Fe in the air can partially remove excess Fe and improve superconductivity in $\text{Fe}_{1+y}\text{Te}_{1-x}\text{Se}_x$.⁶ Air annealing, or incorporation of oxygen during growth, of nonsuperconducting Fe_{1+x}Te thin films also induces superconductivity.^{7–10} The previous works suggest oxygen incorporation for the induced superconductivity and excess Fe for the suppression of superconductivity. However, the roles of oxygen in these materials, whether it is due to substitution or interstitial occupation, are not clear.

Here, we report a structural investigation of oxygen-annealed nonsuperconducting single crystal $\text{Fe}_{1.08}\text{Te}_{0.55}\text{Se}_{0.45}$ with the PbO-type structure. The $\text{Fe}_{1.08}\text{Te}_{0.55}\text{Se}_{0.45}$ was selected for study because $\text{FeTe}_{0.55}\text{Se}_{0.45}$ without the excess Fe is an optimum doped superconductor, and the study of oxidation in samples with superconductivity suppressed by the excess Fe gives insight to the roles of both oxygen and the excess Fe. The use of bulk single crystals also eliminates the effect of substrate and its strain in thin films. For $\text{Fe}_{1.08}\text{Te}_{0.55}\text{Se}_{0.45}$, the crystal exhibits superconductivity after being annealed in oxygen atmosphere. Dark field (DF) images

in transmission electron microscopy (TEM) and high-angle annular dark-field (HAADF) images in scanning transmission electron microscopy (STEM) demonstrate that the hexagonal NiAs-type phases of Fe(Te/Se) are formed in local areas. STEM-HAADF imaging shows that the sample homogeneity is also improved in the remaining PbO-type phase after oxygen annealing. Oxygen was detected by using electron energy loss spectroscopy (EELS); the fine structure of the O-K edge shows a prepeak resulting from p-d hybridization of O 2p and Fe 3d valence states. The average L_3/L_2 intensity ratio of the Fe- $L_{2,3}$ edge increases from 5.27 in the as-grown sample to 5.85 in the oxygen-annealed sample, indicating an increase in the Fe valence towards 3+.

II. EXPERIMENT

Single crystals of $\text{Fe}_{1.08}\text{Te}_{0.55}\text{Se}_{0.45}$ were grown by a unidirectional solidification method and under a slow cool down procedure.¹¹ High resolution synchrotron powder diffraction data were collected at room temperature using beam-line 11-BM with an incident x-ray beam of 0.4134 Å wavelength at the Advanced Photon Source (APS), Argonne National Laboratory. STEM and EELS were performed using the JEOL2200FS, while electron nanodiffraction was carried using JEOL2010F. Both microscopes are installed at the University of Illinois. The JEOL2200FS is equipped with a CEOS probe corrector and an in-column Ω -energy filter, which is used for EELS. Both microscopes were operated at 200 kV. The TEM samples were prepared using the procedure reported in Ref. 12.

III. RESULTS AND DISCUSSION

The as-grown sample of $\text{Fe}_{1.08}\text{Te}_{0.55}\text{Se}_{0.45}$ was annealed at 120 °C in 500 mTorr O_2 atmosphere for 90 minutes. The overall measured composition of the sample, $\text{Fe}_{1.10}\text{Te}_{0.54}\text{Se}_{0.46}$, as detected by inductively coupled plasma (ICP) mass spectroscopy, remains the same before and after annealing. The amount of excess Fe detected by ICP is slightly higher than the nominal composition, and the concentration of Te and Se

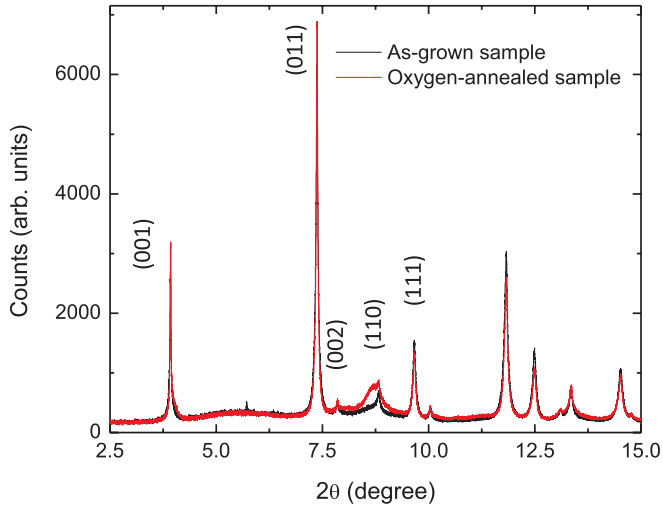


FIG. 1. (Color online) Synchrotron powder diffraction of as-grown and oxygen-annealed samples shown in black and red, respectively.

varies a little. Synchrotron powder diffractions of as-grown and annealed samples revealed very little change in the crystal lattice constants. Changes in the powder diffraction intensity were observed, as shown in Fig. 1. Refinement of the powder diffraction data suggests that the excess Fe move away from the Fe-Te(Se) layer after annealing, but the result is not conclusive. A large increase in the peak width of reflection (110) was also observed after annealing. The four-probe resistivity measurements were performed on the as-grown and oxygen annealed samples, respectively. The temperature dependence of resistivity for the as-grown sample is shown as the dashed curve in the Fig. 2. No zero resistivity was observed, but trace of superconductivity is suggested by the large drop in resistivity. The temperature dependence of the resistivity for the oxygen annealed sample is plotted as the solid curve in the Fig. 2, which demonstrates superconducting transition around 14.5 K and zero resistivity around 11.5 K. The inset of Fig. 2 shows the enlargement of the resistivity-temperature curves.

We noticed that exposure to air at room temperature also makes the as-grown sample superconducting, although both the T_c is not as high as, and the transition width is not as sharp as, that after oxygen annealing. For the as-grown sample, we cleaved and took a piece from the middle of a thick crystal to ensure that it did not expose to air directly. The edges of the cleaved sample were also cut off to minimize oxidation effect for the $R(T)$ curve measurement. The drop in resistance observed in the as-grown sample, nonetheless in some part, could be still due to the residual diffused in oxygen. We also annealed the as-grown sample in vacuum at 140 °C for 180 minutes, and no significant change in the $R(T)$ curve was seen, which indicates oxygen plays an important role in improvement of superconductivity.

TEM samples with uniform thickness in a relative large area (~ 100 nm) were prepared from the as-grown crystals using a tape method described elsewhere.¹² The above oxygen annealing procedure was carried out for the TEM sample. Figure 3(a) shows an electron diffraction pattern along the [001] zone axis of the oxygen-annealed $\text{Fe}_{1.08}\text{Te}_{0.55}\text{Se}_{0.45}$

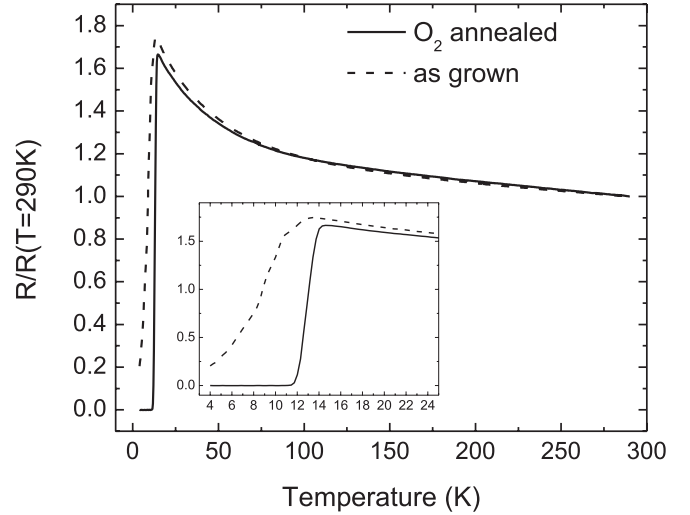


FIG. 2. Temperature dependence of resistivity for the as-grown and oxygen-annealed single crystal $\text{Fe}_{1.08}\text{Te}_{0.55}\text{Se}_{0.45}$ shown as the dashed and solid curve, respectively, demonstrating the emergence of superconductivity in the nonsuperconducting crystal after oxygen annealing.

sample, recorded on the Fuji image plate by using JEOL 2010F (JEOL, USA). In addition to the reflections arranged in the square pattern belonging to the tetragonal PbO-type phase ($P4/nmm$), extra reflections appear in the diffraction pattern. The reflection (200) of the tetragonal phase is labeled with a subscript T as (200)_T. Some of these additional reflections are identified as two sets of diffraction patterns of the hexagonal NiAs-type Fe(Te/Se) phase ($P63/mmc$) along [001] direction, with difference in orientation by 30°. The reflections (100), (010), and (110) of the hexagonal phase are labeled with a subscript of H.a and H.b for these two sets of diffraction patterns, respectively. The inset in Fig. 3(a) shows the enlarged

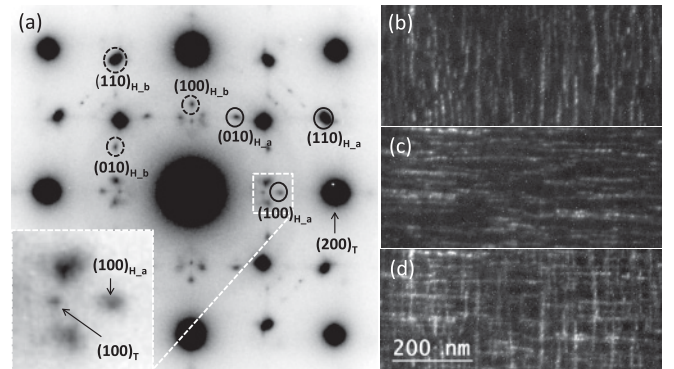


FIG. 3. (a) An electron diffraction pattern of the oxygen-annealed $\text{Fe}_{1.08}\text{Te}_{0.55}\text{Se}_{0.45}$ along [001] direction, demonstrating mixed phases. Reflections of the tetragonal PbO-type phase are labeled with subscript T. Two sets of diffraction patterns of the hexagonal NiAs-type phase are indexed with subscript H.a and H.b, respectively. The inset shows the enlarged pattern from the boxed region. Two DF images, formed from the reflections of (110)_{H.a} and (110)_{H.b}, are shown in (b) and (c), respectively, which show the needle-like contrast aligning with a and b axis of the tetragonal phase, respectively. A combined DF image by adding (b) and (c) is shown in (d) showing the meshlike contrast.

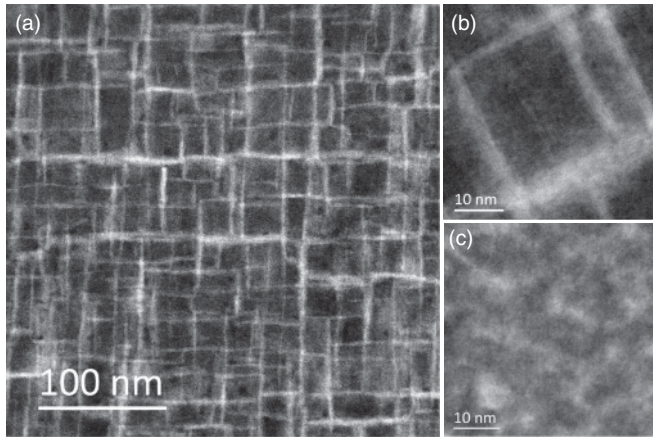


FIG. 4. (a) A HAADF image of the oxygen-annealed $\text{Fe}_{1.08}\text{Te}_{0.55}\text{Se}_{0.45}$ along [001] direction at low magnification. An enlarged image of the oxygen-annealed sample is shown in (b). For comparison, a HAADF image of the as-grown $\text{Fe}_{1.08}\text{Te}_{0.55}\text{Se}_{0.45}$ demonstrating spinodal decomposition is shown in (c).

pattern from the boxed region. For the tetragonal PbO-type phase, reflections $h + k = \text{odd}$ are seen [reflection $(100)_T$ is labeled]. These reflections are expected to be extinct in the terminal phases of FeSe and FeTe with the tetragonal symmetry of $P4/nmm$ or when Se and Te are randomly mixed. In the as-grown sample, those reflections were also noticed, which was interpreted by a small separation in the occupancy, or preference, of the two Te/Se sites inside the tetragonal unit cell by Se and Te atoms, respectively, leading to a net scattering for the $h + k = \text{odd}$ reflections. In the insert of Fig. 3(a) there are two other broad reflections that are not identified yet.

Two DF images, shown in Figs. 3(b) and 3(c), were formed by selecting the reflections of $(110)_{h-a}$ and $(110)_{h-b}$ in Fig. 3(a), respectively. The contrast in the DF images has the appearance of being needlelike, which aligns with a and b axis of the tetragonal phase, respectively, indicating that the hexagonal phases are coherent with the tetragonal phase. Figure 3(d) demonstrates a combined DF image by adding Figs. 3(b) and 3(c) together, showing a meshlike contrast. Based on the powder diffraction file (PDF) database, lattice constant a of tetragonal and hexagonal phases are close with a mismatch of at most about 3% in FeSe and less than 1% in FeTe, which explains the lattice coherence between the hexagonal and tetragonal phases in the a - b plane. The lattice along the c -axis direction is expected to be incoherent with a mismatch as large as around 10% based on the PDF data between tetragonal and hexagonal phases. The formation of the hexagonal phase is expected to result in significant strain in the oxygen-annealed sample.

The STEM and EELS experiments were performed on a JEOL 2200FS (JEOL, USA) microscope equipped with a CEOS spherical aberration corrector (CEOS GmbH). The microscope was operated at 200 keV.¹³ Figure 4(a) shows a HAADF image at low magnification. The image shows the similar meshlike contrast, as seen in Fig. 3(d), which suggests the hexagonal phases mainly exist in the brighter regions in the HAADF image. In STEM, incoherently scattered intensities, collected by the HAADF detector with a large inner-cutoff angle, are proportional to thickness and power of atomic num-

bers. The tetragonal phase has 22 Te/Se atoms per nm^3 , while there are 28 Te/Se atoms per nm^3 in the hexagonal phase. The density difference explains the contrast seen in the HAADF image. Low-loss EELS analysis shows that the plasmon loss in the hexagonal phases shifts to higher energy by about 0.7 eV compared to the remaining tetragonal phase, which suggests the difference in the density of free carriers in the two phases. Figure 4(b) shows an enlarged HAADF image, which exhibits no contrast of spinodal decomposition that was observed in the as-grown sample [see Fig. 3(c)].¹² Similar phase separation in the as-grown $\text{FeTe}_{0.55}\text{Se}_{0.45}$ was also reported by X. He *et al.* via scanning tunneling microscopy.¹⁴ Although the image intensity variation in the oxygen-annealed sample was still observable, the extent of the variation is much smaller than that in the as-grown sample. This observation indicates sample homogeneity was improved after oxygen annealing in the tetragonal phase.

The hexagonal NiAs-type FeSe phase was often detected as impurity in the tetragonal PbO-type FeSe superconductor.^{5,15–17} It has been reported that this tetragonal phase slowly converts to the hexagonal phase below 300 °C.⁵ The hexagonal NiAs-type FeTe phase, normally with Fe deficiency, has also been reported.¹⁸ However, we found no evidence of hexagonal phases in as-grown $\text{Fe}_{1+y}\text{Te}_{1-x}\text{Se}_x$ single crystals.¹² Thus, the observed hexagonal phase is the result of oxygen annealing. Neither hexagonal NiAs-type FeSe or FeTe phase exhibits superconductivity.^{5,19} This structure consists of Fe in a hexagonal lattice with Se/Te atoms occupying the alternating sites of the Fe lattice. The structure lacks the two-dimensional FeSe/Te layer structure, which is believed to be the active layer that is critical in iron-based superconductors.

In what follows, we focus on the STEM-EELS characterization of the superconducting tetragonal phase. Figure 5(a) shows a typical EELS spectrum with O-K, Te-M_{4,5}, and Fe-L_{2,3} edges labeled. The background-subtracted experimental O-K edge is shown in Fig. 5(b) by open symbols; the solid curve, obtained by smoothing the experimental data, is for the guidance of eyes, which demonstrates three peaks labeled (a)–(c). The prepeak (a) around 530 eV indicates hybridizing of Fe 3d and oxygen 2p orbitals.²⁰ C. Colliex *et al.* systematically investigated O-K edges in FeO, Fe₃O₄, α -Fe₂O₃, and γ -Fe₂O₃.²⁰ They demonstrated that both Fe₃O₄ and γ -Fe₂O₃ show a small distinct peak in between (b) and (c), which is absent in the fine structure of the O-K edge we observed. The prepeak (a) we observed, thus, appears as a mixture of the prepeaks in FeO and α -Fe₂O₃ in terms of the relative prepeak intensity. The fine structure of O-K edges in FeO and α -Fe₂O₃ are reproduced from Ref. 20 and plotted in Fig. 5(c) for comparison. Next, the fine structure of the Fe-L_{2,3} edge was analyzed. In the as-grown sample, our previous work shows that the L_3/L_2 intensity ratio fluctuates between 4.3 and 5.8 observed in Te-rich and Te-poor phases, respectively.¹² The averaged L_3/L_2 intensity ratio of the as-grown sample measured here was calculated by averaging spectra acquired at different sample positions and was found to be 5.27 ± 0.09 . The details of the calculation method for the L_3/L_2 intensity ratio were reported elsewhere.¹² A separate EELS experiment for the as-grown sample in the TEM mode did

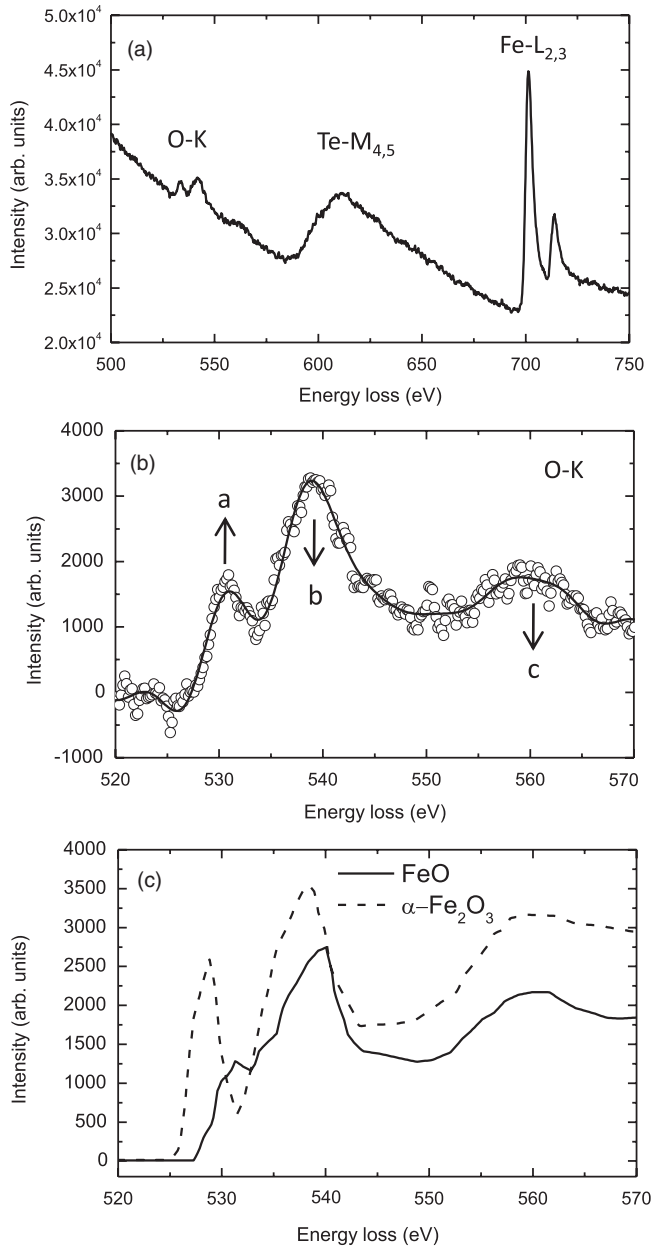


FIG. 5. (a) A typical EELS spectrum with O-K, Te-M_{4,5}, and Fe-L_{2,3} edges labeled. (b) The background subtracted experimental data of the O-K edge are shown as the open symbols. The solid curve, obtained by smoothing the experimental data, shows three peaks (a)–(c) indicated by the arrows, respectively. The prepeak (a) indicates hybridization of Fe 3d and O 2p states. (c) Fine structure of FeO and α -Fe₂O₃, reproduced from Ref. 19. The prepeak (a) we observed looks like mixture of that in FeO and α -Fe₂O₃.

not detect oxygen in the thicker sample regions, while very small amounts of oxygen signals were seen in the thinner sample regions, indicating oxygen only diffuses into surface layers in as-grown samples. For the annealed sample, the same procedure gives 5.85 ± 0.14 for the L₃/L₂ intensity ratio of the Fe-L_{2,3} edge in the superconducting, tetragonal phase, which represents an increase of 0.58 over the as-grown sample.

Improvement of bulk superconductivity has been previously reported in the Fe_{1+y}Te_{1-x}Se_x with smaller amount of excess Fe after annealing in air at 270 °C; the improvement was attributed to partial removal of excess Fe.⁶ In our study the as-grown single crystal of Fe_{1.08}Te_{0.55}Se_{0.45} with large amount of excess Fe exhibits no superconductivity due to excess Fe but becomes superconducting after annealing in oxygen atmosphere at low temperatures. Analysis revealed no overall change in sample composition. Fe deficiency is often found in the hexagonal NiAs-type FeSe²¹ and FeTe,¹⁸ respectively, which suggests that the excess Fe likely to remain in the tetragonal phase if not removed. The role of oxygen annealing has been studied theoretically. Y. Nie *et al.* performed the density functional calculations with the projector augmented wave method as implemented in VASP code.^{10,22} A $2 \times 2 \times 1$ supercell of FeTe was built with interstitial oxygen partially located at symmetric sites of Te. The projected density of state was calculated for a different number of interstitial oxygen varying from 1 to 4 in the supercell corresponding to FeTeO_x with $x = 0.125, 0.25, 0.375$, and 0.5. They found that Fe d states and O p states have the strongest hybridization in FeTeO_{0.5} corresponding to nominal Fe valence of 3+, and the Fermi surface is also strongly affected. The density functional calculation performed by L. Zhang *et al.* shows that the excess Fe is strongly magnetic and acts as an electron donor to the Fe layers,²³ which is responsible for the suppression of superconductivity and induction of weakly localized electronic states.²⁴ C. Dong *et al.*⁶ suggested that excess Fe could be partially removed as implied by energy-dispersive x-ray spectroscopy as well as color change from black to red-brown, indicating the existence of iron oxide. However, we did not see evidences of iron oxide. Atomic force microscopy (AFM) images in Fig. 6 also show largely smooth surface in our as-grown and oxygen-annealed samples, except spots separated by hundreds of nm in distances. Density of such white spots increased slightly after oxygen annealing.

The Fe valence can be measured experimentally as previous systematic investigations of the L_{2,3} edges of 3d transition-metal oxides, which reveals a strong correlation between the L₃/L₂ intensity ratio and the d-state occupancy.^{25,26} According to these studies, the L₃/L₂ intensity ratio of Fe-L_{2,3} increases as Fe valence increases from 2+ to 3+. Our EELS result shows an increase in the L₃/L₂ intensity ratio of the oxygen-annealed sample by 0.58 compared to the ratio of 5.27 in the as-grown sample, indicating an increase in the oxidation state. This is consistent with the previous report in the oxygen-annealed FeTe thin film measured by x-ray absorption spectroscopy.^{7,9} Improvement of superconductivity was also observed in the FeTe_{1-x}S_x annealed in oxygen at 200 °C by Y. Mizuguchi *et al.*,^{27,28} who also attribute the evolution of superconductivity to suppression of local moment of excess Fe by oxygen annealing. They also found the induced superconductivity by oxygen incorporation is suppressed when the oxygen-annealed sample is annealed again in vacuum, suggesting that the excess Fe remained in the sample. A similar effect of oxygen annealing on FeTe_{1-x}S_x was also reported by V.P.S. Awana *et al.*²⁹ Although no Fe-valence measurement has been reported in the sulfur-doped system yet, one may also expect an increase in Fe valence in the oxygen-annealed FeTe_{1-x}S_x. Improvement of superconductivity induced by oxidation of Fe

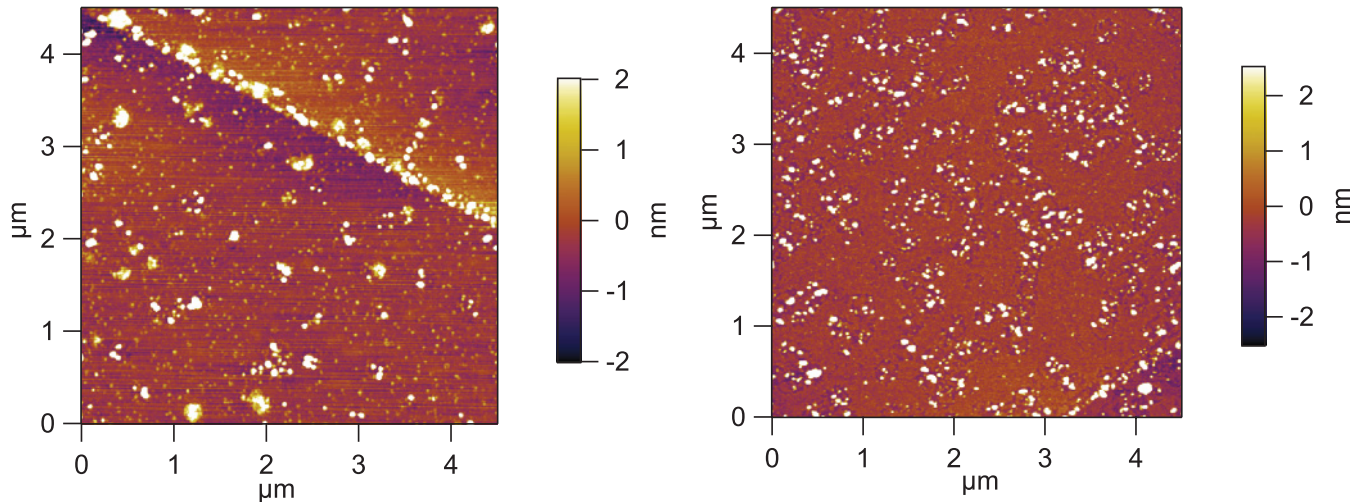


FIG. 6. (Color online) AFM images of as-grown and oxygen-annealed samples shown in (a) and (b), respectively.

in iron chalcogenide suggests superconductivity is favorable to higher Fe valence with suppression of the effect of excess Fe.

Hexagonal phases are normally associated with Fe deficiency, as reported earlier.^{21,30} Oxygen, in the same column of Te/Se, has a stronger electronegativity. We speculate that oxygen atoms bond with Fe making the Fe-Te/Se bonding weaker or even broken, resulting in Fe deficiency in local areas. This and the fact that the hexagonal phase as a more stable phase at low temperatures, as shown in Ref. 5, provide the driving force and the pathway for the formation of the hexagonal phases. In our experiment with annealing in vacuum, the hexagonal phase did not form during the short period of annealing, although the hexagonal phase is expected based on the phase diagram consideration. This observation supports the previous suggestion that the oxygen plays a role in speeding up the phase transformation.

IV. CONCLUSIONS

In summary, we investigated the effect of oxygen annealing in the nonsuperconducting single crystal $\text{Fe}_{1.08}\text{Te}_{0.55}\text{Se}_{0.45}$. Although the as-grown sample shows no superconductivity, the oxygen-annealed sample was found to show an onset T_c around 14.5 K, which is close to that in the optimally doped

superconductor. Phase transformation from the tetragonal PbO -type phase to the hexagonal NiAs -type phase in the oxygen-annealed sample was found in local areas forming meshlike contrast, observed by using DF imaging and STEM-HAADF imaging. Such precipitates of the hexagonal phases formed in the matrix of the tetragonal phases could be significant for improvement on the critical current density J_c and its isotropy. Improvement of homogeneity in the tetragonal phase was observed by STEM-HAADF imaging. There is an increase in the Fe valence in the oxygen-anneal sample, which is consistent with oxygen doping as evidenced by EELS.

ACKNOWLEDGMENTS

This material is based upon work supported as part of the Center for Emergent Superconductivity, an Energy Frontier Research Center funded by the US Department of Energy, Office of Science, Office of Basic Energy Sciences, under award number DE-AC0298CH10886. Use of the Advanced Photon Source at Argonne National Laboratory was supported by the US Department of Energy, Office of Science, Office of Basic Energy Sciences under Contract No. DE-AC02-06CH11357. We sincerely thank D. Gray of UIUC for help with the analysis of synchrotron powder diffraction data.

*jianzuo@illinois.edu

¹Y. Kamihara, T. Watanabe, M. Hirano, and H. Hosono, *J. Am. Chem. Soc.* **130**, 3296 (2008).

²K. W. Yeh, T. W. Huang, Y. L. Huang, T. K. Chen, F. C. Hsu, P. M. Wu, Y. C. Lee, Y. Y. Chu, C. L. Chen, J. Y. Luo, D. C. Yan, and M. K. Wu, *EPL* **84**, 37002 (2008).

³W. Bao, Y. Qiu, Q. Huang, M. A. Green, P. Zajdel, M. R. Fitzsimmons, M. Zhernenkov, S. Chang, M. H. Fang, B. Qian, E. K. Vehstedt, J. H. Yang, H. M. Pham, L. Spinu, and Z. Q. Mao, *Phys. Rev. Lett.* **102**, 247001 (2009).

⁴M. Bendele, P. Babkevich, S. Katrych, S. N. Gvasaliya, E. Pomjakushina, K. Conder, B. Roessli, A. T. Boothroyd, R. Khasanov, and H. Keller, *Phys. Rev. B* **82**, 212504 (2010).

⁵T. M. McQueen, Q. Huang, V. Ksenofontov, C. Felser, Q. Xu, H. Zandbergen, Y. S. Hor, J. Allred, A. J. Williams, D. Qu, J. Checkelsky, N. P. Ong, and R. J. Cava, *Phys. Rev. B* **79**, 014522 (2009).

⁶C. Dong, H. Wang, Z. Li, J. Chen, H. Q. Yuan, and M. Fang, *Phys. Rev. B* **84**, 224506 (2011).

⁷Y. F. Nie, D. Telesca, J. I. Budnick, B. Sinkovic, and B. O. Wells, *Phys. Rev. B* **82**, 020508 (2010).

⁸W. D. Si, Q. Jie, L. J. Wu, J. Zhou, G. D. Gu, P. D. Johnson, and Q. Li, *Phys. Rev. B* **81**, 092506 (2010).

⁹D. Telesca, Y. Nie, J. I. Budnick, B. O. Wells, and B. Sinkovic, e-print [arXiv:1102.2155v1](https://arxiv.org/abs/1102.2155v1).

- ¹⁰Y. F. Nie, D. Telesca, J. I. Budnick, B. Sinkovic, R. Ramprasad, and B. O. Wells, *Journal of Physics and Chemistry of Solids* **72**, 426 (2011).
- ¹¹J. S. Wen, G. Y. Xu, Z. J. Xu, Z. W. Lin, Q. Li, W. Ratcliff, G. Gu, and J. M. Tranquada, *Phys. Rev. B* **80**, 104506 (2009).
- ¹²H. F. Hu, J. M. Zuo, J. S. Wen, Z. J. Xu, Z. W. Lin, Q. Li, G. D. Gu, W. K. Park, and L. H. Greene, *New J. Phys.* **13** (2011).
- ¹³J. G. Wen, J. Mabon, C. H. Lei, S. Burdin, E. Sammann, I. Petrov, A. B. Shah, V. Chobpattana, J. Zhang, K. Ran, J. M. Zuo, S. Mishina, and T. Aoki, *Microscopy and Microanalysis* **16**, 183 (2010).
- ¹⁴X. B. He, G. R. Li, J. D. Zhang, A. B. Karki, R. Y. Jin, B. C. Sales, A. S. Sefat, M. A. McGuire, D. Mandrus, and E. W. Plummer, *Phys. Rev. B* **83**, 220502 (2011).
- ¹⁵Y. J. Xia, F. Q. Huang, X. M. Xie, and M. H. Jiang, *Europhys. Lett.* **86**, 37008 (2009).
- ¹⁶F. C. Hsu, J. Y. Luo, K. W. Yeh, T. K. Chen, T. W. Huang, P. M. Wu, Y. C. Lee, Y. L. Huang, Y. Y. Chu, D. C. Yan, and M. K. Wu, *Proc. Nat. Acad. Sci. USA* **105**, 14262 (2008).
- ¹⁷Y. Hara, K. Takase, A. Yamasaki, H. Sato, N. Miyakawa, N. Umeyama, and S. I. Ikeda, *Physica C* **470**, S313 (2010).
- ¹⁸M. Ellner, *J. Less-Common Met.* **48**, 21 (1976).
- ¹⁹A. K. Yadav, A. D. Thakur, and C. V. Tomy, *Solid State Commun.* **151** (2011).
- ²⁰C. Colliex, T. Manoubi, and C. Ortiz, *Phys. Rev. B* **44**, 11402 (1991).
- ²¹G. Hagg and A. L. Kindstrom, *Z. Phys. Chem.* **22**, 453 (1933).
- ²²Y. Nie, Ph.D. dissertation, University of Connecticut, 2011.
- ²³L. J. Zhang, D. J. Singh, and M. H. Du, *Phys. Rev. B* **79**, 012506 (2009).
- ²⁴T. J. Liu, X. Ke, B. Qian, J. Hu, D. Fobes, E. K. Vehstedt, H. Pham, J. H. Yang, M. H. Fang, L. Spinu, P. Schiffer, Y. Liu, and Z. Q. Mao, *Phys. Rev. B* **80**, 174509 (2009).
- ²⁵T. G. Sparrow, B. G. Williams, C. N. R. Rao, and J. M. Thomas, *Chem. Phys. Lett.* **108**, 547 (1984).
- ²⁶J. Graetz, C. C. Ahn, H. Ouyang, P. Rez, and B. Fultz, *Phys. Rev. B* **69**, 235103 (2004).
- ²⁷Y. Mizuguchi, K. Deguchi, S. Tsuda, T. Yamaguchi, and Y. Takano, *Europhys. Lett.* **90**, 57002 (2010).
- ²⁸Y. Mizuguchi, K. Deguchi, Y. Kawasaki, T. Ozaki, M. Nagao, S. Tsuda, T. Yamaguchi, and Y. Takano, *J. Appl. Phys.* **109**, 013914 (2011).
- ²⁹V. P. S. Awana, A. Pal, A. Vajpayee, B. Gahtori, and H. Kishan, *Physica C* **471**, 77 (2011).
- ³⁰F. Gronvold, H. Haraldsen, and J. Vihovde, *Acta Chem. Scand.* **8**, 1927 (1954).